Spectral–Spatial Anomaly Detection of Hyperspectral Data Based on Improved Isolation Forest

Xiangyu Song, Sunil Aryal, *Member, IEEE*, Kai Ming Ting, Zhen Liu, and Bin He

***Abstract*— Anomaly detection in hyperspectral image (HSI) is affected by redundant bands and the limited utilization capacity of spectral–spatial information. In this article, we propose a novel improved Isolation Forest (IIF) algorithm based on the assumption that anomaly pixels are more susceptible to isolation than background pixels. The proposed IIF is a modified version of the Isolation Forest (iForest) algorithm, which addresses the poor performance of iForest in detecting local anomalies and anomaly detection in high-dimensional data. Furthermore, we propose a spectral–spatial anomaly detector based on IIF (SSIIFD) to make full use of global and local information, as well as spectral and spatial information. To be specific, first, we apply the Gabor filter to extract spatial features, which are then employed as input to the relative mass isolation forest (ReMass-iForest) detector to obtain the spatial anomaly score. Next, original images are divided into several homogeneous regions via the entropy rate segmentation (ERS) algorithm, and the preprocessed images are then employed as input to the proposed IIF detector to obtain the spectral anomaly score. Finally, we fuse the spatial and spectral anomaly scores by combining them linearly to predict anomaly pixels. The experimental results on four real hyperspectral datasets demonstrate that the proposed detector outperforms other state-of-the-art methods.**

***Index Terms*— Anomaly detection, hyperspectral image (HSI), isolation forest (iForest), spectral–spatial information.**

I. Introduction

HYPERSPECTRAL image (HSI) with hundreds of contiguous bands for each pixel can provide abundant spectral and spatial information simultaneously [1]. HSI has been widely applied in many remote sensing applications, such as anomaly detection [2], [3], classification [4], and change detection [5]. Among these applications, hyperspectral anomaly detection has received extensive attention. A wide variety of methods have been developed, which aims at distinguishing outliers, whose spectral and spatial signatures are highly distinct from their surrounding pixels or the global background in an unsupervised way.

In the literature, most methods have concentrated on examination of the role of HSI spectral signatures in anomaly detection, employing exclusively the spectrum of a given pixel to determine its outlier status. The statistical model-based technique is the first category in hyperspectral anomaly detection. One of the most well-known methods is the Reed–Xiaoli (RX) algorithm, proposed by Reed and Yu [6], which is considered as the main benchmark method. The RX detector (RXD) assumes that the background can be modeled by employing multivariate Gaussian distributions. The RX detector has two versions, i.e., the global RX and local RX (LRXD), where LRXD models the background with neighborhood pixels. However, most real-world HSIs cover different classes of materials and exhibit complex backgrounds, which mean that the Gaussian distribution assumption is oversimplified in real-world HSIs. Therefore, several variants of the RX detector have been proposed [7]–[12]. For example, the kernel RX [7] detector is a nonlinear version of the RXD, which calculates the Mahalanobis distance between the pixels to be tested and the background in higher dimensional feature space with the kernel theory. The cluster-based anomaly detector (CBAD) [8] segments the whole HSI into several clusters and then detects anomalies in each cluster with the RX detector. Zhou *et al.* [12] proposed a novel cluster kernel RX detector to accelerate the kernel RX detector by partitioning the whole HSI into several clusters and then employing a fast eigenvalue decomposition algorithm to obtain detection results.

In addition to statistical model-based methods, there are many other types of detectors. For example, the orthogonal subspace projection (OSP) is a typical geometrical modeling-based method. Chang *et al.* [54], [55] developed OSP-based techniques and obtained good results. Another example, the low-rank and sparse representation detector (LRASR) is proposed in [13], which exploits the low-rank property of background pixels to distinguish sparse pixels. The background joint sparse representation (BJSR) [14] detector is a representation-based method that selects the most

Manuscript received July 12, 2021; accepted August 11, 2021. Date of publication August 24, 2021; date of current version January 26, 2022. This work was supported in part by the National Natural Science Foundation of China (NSFC) under Grant 61801455 and in part by the National Natural Science Foundation of Jilin Province under Grant YDZJ202101ZYTS048. *(Corresponding author: Bin He.)*

Xiangyu Song is with Changchun Institute of Optics, Fine Mechanics and Physics, Chinese Academy of Sciences (CIOMP), Changchun 130033, China, and also with the School of Optoelectronics, University of Chinese Academy of Sciences, Beijing 100049, China (e-mail: songxiangyu17@mails.ucas.edu.cn).

Sunil Aryal is with the School of Information Technology, Deakin University, Waurn Ponds, VIC 3216, Australia (e-mail: sunil.aryal@deakin.edu.au).

Kai Ming Ting is with the National Key Laboratory for Novel Software Technology, Nanjing University, Nanjing 210023, China (e-mail: tingkm@nju.edu.cn).

Zhen Liu is with the Big Data Research Center and the Web Sciences Center, School of Computer Science and Engineering, University of Electronic Science and Technology of China, Chengdu 611731, China (e-mail: quake@uestc.edu.cn).

Bin He is with the Changchun Institute of Optics, Fine Mechanics and Physics, Chinese Academy of Sciences (CIOMP), Changchun 130033, China (e-mail: hebin@ciomp.ac.cn).

Digital Object Identifier 10.1109/TGRS.2021.3104998

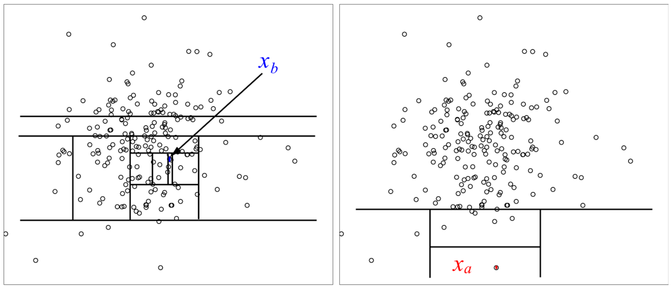

(a) (b)

Fig. 1. Graphical example illustrating the principle of iTrees given a Gaussian distribution of 205 points. (a) Anomaly instance, x_a, is isolated through only four random partitions. (b) Normal instance, x_b, requires 11 random partitions to be isolated.

representative background bases with the joint sparsity model, and background pixels are then suitably represented with the selected bases, whereas anomaly pixels cannot be represented. Similarly, collaborative representation-, sparse representation-, and tensor representation-based anomaly detectors have also received substantial attention. For example, in [50], a collaborative representation-based detector (CRD) was proposed to detect anomalies with unknown signatures, and a pixel is claimed to be an anomaly if it cannot be collaboratively represented by background atoms in a local window. Another example, the prior-based tensor approximation (PTA) detector is a typical tensor representation-based method proposed in [15], which combines priors (i.e., low rank, sparse, and piecewise smooth) with the advantages of the tensor representation of HSIs. Then, the priors are embedded into the dimensions of a tensor with different regularizations according to certain physical meanings to preserve the global structure while increasing the gap between anomaly and background pixels. In addition, since the spatial resolution of HSI is increasing, the complementarity of spectral and spatial domains can further improve detection performance [38], [47], and [49]. Moreover, hyperspectral anomaly detectors based on support vector data description (SVDD) [16], [17], game theory [56], morphological and attribute filters [18], [19], deep learning [20]–[23], and so on, have been investigated as well.

Additionally, Li *et al.* [24], [25] proposed a novel kernel isolation forest-based detector (KIFD) according to the isolation forest (iForest) algorithm [26], [27] 2 years ago. This was the first time that iForest was introduced into remote sensing applications. Subsequently, Wang *et al.* [28] established a hyperspectral anomaly detector that combined multiple features and iForest (MFIFD) last year. Both methods have been demonstrated to perform well.

Although both the KIFD and MFIFD have been revealed to perform well in hyperspectral anomaly detection, we have identified certain weaknesses of iForest in detecting anomalies in high-dimensional data and detecting local anomalies. Specifically, iForest cannot detect local anomalies because the path length measures the degree of anomaly globally. In addition, only one data dimension is randomly selected in every partition, which reduces the reliability of the algorithm, as we will see later in Section II-A of this article. The basic motive of our research is to enhance the detection accuracy by overcoming those two limitations of iForest-based anomaly detectors in hyperspectral anomaly detection. We propose a new improved isolation forest (IIF) algorithm. Furthermore, in this article, a novel spectral–spatial IIF-based detection framework (SSIIFD) is developed. Specifically, the main contributions of this article are as follows:

1) An SSIIFD is proposed, which can make full use of the spectral and spatial information, and the global and local information of HSIs.

2) An IIF algorithm is proposed for the first time which effectively improves the poor performance of iForest in the detection of anomalies in high-dimensional data and local anomaly detection.

3) Experiments on four real datasets demonstrate that the proposed SSIIFD can obtain the best detection accuracy.

The remainder of this article is organized as follows. Section II briefly reviews the iForest and its two variations; the extraction of spatial features with the Gabor filter and the entropy rate superpixel segmentation (ERS) algorithm are briefly reviewed in this section. The proposed method is introduced in detail in Section III. In Section IV, experimental results are presented. Finally, a conclusion is drawn in Section V.

II. Related Works

A. Isolation Forest and Its Two Variations

The iForest introduced by Liu *et al.* [26], [27] is an outlier detector that does not employ distance or density measures. It builds an ensemble of isolation trees (iTrees) for a given dataset. The main advantage of this algorithm is that it does not rely on a determined profile representing the data to find samples that do not conform to this profile. Rather, it utilizes the fact that anomalies are "few and different," which makes them more susceptible to isolation in a binary tree structure than normal points. Hence, anomalies are isolated closer to the root of the tree, whereas normal points are isolated toward the deeper end of the tree. In other words, anomalies exhibit shorter average path lengths than those of normal points over a collection of iTrees. Here, the principle of iForest is briefly reviewed. For more details of the iForest algorithm, we refer readers to [26] and [27].

Specifically, in an iForest, data are subsampled and processed in a tree structure based on random cuts in the values of arbitrarily selected features in a given dataset. Each tree is grown until each instance is isolated into a leaf node. Those samples that travel deeper into the tree branches are less likely to be anomalous, whereas shorter branches are indicative of anomalies. As such, the aggregated lengths of the tree branches provide a measure of the occurring anomalies or an anomaly score for every given point. To demonstrate that anomalies are more susceptible to isolation under random partitioning, an example of the random partitioning process of a normal point versus an anomaly is shown in Fig. 1. We observe that a normal instance, x_b, generally requires more separating lines to be isolated, while an anomaly instance, x_a, generally requires less separating lines to be isolated.

On the one hand, unsatisfactory results have often been achieved when employing iForest in the detection of local anomalies in datasets containing multiple clusters of normal instances because the local anomalies are masked by those normal clusters of similar density. Hence, they become less susceptible to isolation via iTrees. In other words, iForest does not detect local anomalies because the path length globally measures the degree of anomaly. It does not consider the isolation magnitude of an instance from its local neighborhood. To address this problem, Aryal and Ting [29], according to the mass estimation theory [30], developed ReMass-iForest by replacing the global ranking measure based on path length with a local ranking measure based on relative mass that takes local data distribution into consideration. ReMass-iForest applies the same implementation of iTrees as that of iForest. Empirical evaluations have indicated that ReMass-iForest performs better than iForest in terms of the task-specific performance.

On the other hand, only one data dimension is randomly selected in every partition. In other words, the applied branch cuts are simply parallel to the coordinate axes, which results in certain regions, not necessarily containing many data points, ending up with many branch cuts. As such, most dimensions of the data are not considered when building iTrees, which reduces the reliability of the algorithm, especially in regard to high-dimensional problems with a large number of attributes. Hariri *et al.* [31] presented an extension to iForest, namely the extended isolation forest (EIF), by using hyperplanes with random slopes (non-axis-parallel) to split data in the creation of iTrees, which resolves the issues associated with the assignment of anomaly scores to given data points. The results of EIF are more reliable and robust and in some cases more accurate in a given dataset.

iForest, in recent years, has been successfully applied in remote sensing applications. Specifically, iForest was first introduced into the hyperspectral anomaly detection field by Li *et al.* [24], [25]. In addition, Wang *et al.* [28] proposed a hyperspectral anomaly detector combining multiple features and iForest. Although both methods are shown to perform well, the above two weaknesses of iForest in anomaly detection in HSIs (aka high-dimensional data) containing hundreds of spectral bands and multiple clusters of background pixels are still not addressed. In this article, we develop a novel improved iForest method, optimized for hyperspectral anomaly detection, namely IIF-based anomaly detector (IIFD), by combining spatial texture information and spectral characteristics. Details of how the proposed improved-iForest method overcomes these two weaknesses of iForest will be explained in Section III-C of this article.

B. Gabor Filter

The Gabor filter,[1] which is a sinusoidal function modulated by a Gaussian envelope, has been widely adopted in various applications of computer vision and image processing [32], [33]. The Gabor filter captures certain physical structures of an object in an image, such as specific orientation information, based on a spatial convolution kernel. In recent years, Gabor filters have been successfully applied in hyperspectral classification [34], [35]. The most important advantage of Gabor filters is their invariance to rotation, scale, and translation. Furthermore, they are robust against photometric disturbances, such as illumination changes and image noise. Hence, considering these Gabor features, the spatial texture information of HSIs can be effectively represented.

[1]http://en.wikipedia.org/wiki/Gabor_filter

In a 2-D (a, b) coordinate system, the Gabor filter, including real and imaginary components, can be represented as

$$g(a, b;\lambda, \theta, \psi, \sigma, \gamma) = \exp\left(-\frac{a'^2 + \gamma^2 b'^2}{2\sigma^2}\right) \times \exp\left(i\left(2\pi\frac{a'}{\lambda} + \psi\right)\right) \quad (1)$$

where

$$a' = a\cos\theta + b\sin\theta \quad (2)$$

$$b' = -a\sin\theta + b\cos\theta \quad (3)$$

where λ is the wavelength of the sinusoidal factor, θ is the orientation of the normal to the parallel stripes of the Gabor function, ψ is the phase offset, σ is the standard derivation of the Gaussian envelope, and γ is the spatial aspect ratio specifying the ellipticity of the support of the Gabor function. $\psi = 0$ and $\psi = \pi/2$ return the real and imaginary parts, respectively, of the Gabor filter. Parameter σ is determined by λ and spatial frequency bandwidth bw as

$$\sigma = \frac{\lambda}{\pi}\sqrt{\frac{\ln 2}{2}} \times \frac{2^{\mathrm{bw}} + 1}{2^{\mathrm{bw}} - 1}. \quad (4)$$

C. Entropy Rate Superpixel Segmentation

A superpixel segmentation algorithm, as a preprocessing step, should exhibit a low computational complexity and adhere well to the object boundaries. Liu *et al.* [36] proposed the ERS algorithm with the graph topology that maximizes the objective function under the matroid constraint. Specifically, the objective function comprises two components: the entropy rate of a random walk on a graph and a balancing term. The former, entropy rate, encourages the formation of compact and homogeneous clusters, while the latter, balancing function, favors clusters with similar sizes. The matroid is a combinatorial structure that generalizes the concept of linear independence in vector space. Furthermore, in [36], regarding an undirected graph $G = (V, E)$ where V is the vertex set and E is the edge set, the graph is partitioned into a connected subgraph by choosing a subset of edges $A \subseteq E$ such that the resulting graph $G = (V, A)$ consists of smaller connected components or subgraphs. The objective function of the ERS algorithm is optimized with both the entropy rate $H(A)$ and balancing term $B(A)$

$$A^* = \underset{A}{\operatorname{argmax}}\ \operatorname{tr}(H(A) + \mu B(A)), \quad \text{s.t. } A \subseteq E \quad (5)$$

where $\mu \geq 0$ is the weight of the balancing term and $\operatorname{tr}(\cdot)$ denotes the trace of a square matrix. The entropy rate $H(A)$ favors the formation of compact and homogeneous clusters, whereas the balancing term $B(A)$ encourages clusters of similar sizes. A greedy optimization scheme for the problem expressed in (5) is given in [37].

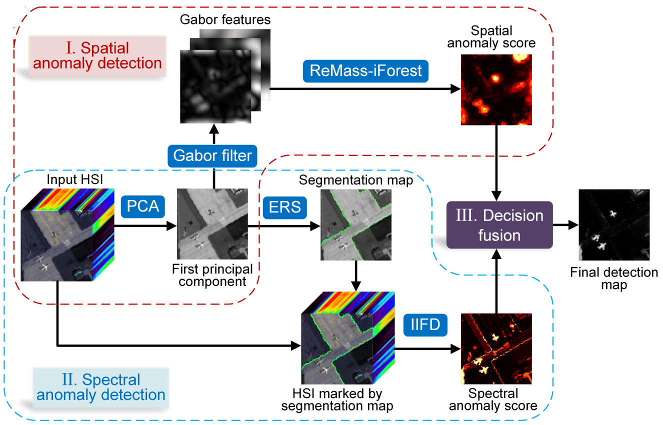

Fig. 2. Architecture for our proposal for hyperspectral anomaly detection with a spectral–spatial joint optimization scheme.

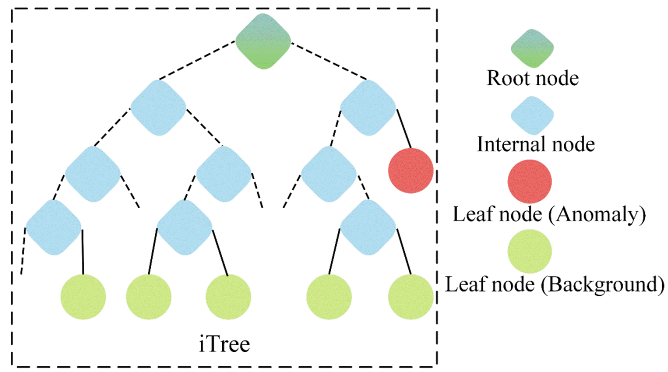

Fig. 3. Example illustrating the structure of an iTree.

III. Proposed Method

Given an HSI, in practical applications, the detection result will be improved when considering both spatial and spectral information [38], which is beneficial for noise suppression and discrimination enhancement between anomalies and the background in HSIs. The proposed SSIIFD framework is designed to detect anomaly pixels by measuring spectral and spatial anomaly scores for every pixel. A schematic of the proposed framework is shown in Fig. 2, which consists of the following three parts:

1) The Gabor filter is applied to extract spatial information from the principal component analysis (PCA)-projected subspace. Gabor features are then employed as the input to the ReMass-iForest detection algorithm to obtain the spatial anomaly score (Part I).

2) The original HSI is divided into several homogeneous regions via the ERS algorithm [36], which are denoted by matrices whose rows are spectral vectors of pixels. The proposed IIFD is then applied to these high-dimensional matrices to obtain the spectral anomaly score (Part II).

3) Finally, we fuse the detection results by linearly combining the obtained spatial and spectral anomaly scores to predict the anomaly pixels given the input HSI (Part III).

A. Gabor Feature Extraction

Let $X \in \mathbb{R}^{N\times D}$ denote the input HSI data, where N is the number of pixels, and D is the number of spectral bands. To extract the Gabor feature [34] of each pixel, we first obtain the projection matrix $P \in \mathbb{R}^{D\times C}$ by solving the following PCA model:

$$\min_{P^T P=I} \operatorname{tr}\left(P^T X^T X P\right) \tag{6}$$

where $I \in \mathbb{R}^{C\times C}$ denotes the identity matrix and $\operatorname{tr}(\cdot)$ denotes the trace of a square matrix. The top C principal components of the HSI are defined as

$$X_{\text{PCA}}^C \in \mathbb{R}^{N\times C} = (X - E(X))P \tag{7}$$

where $E(\cdot)$ denotes the mean function. X_{PCA}^C are then convolved with a Gabor filter [39] with different orientations and scales. Finally, filtering coefficients are extracted as the Gabor feature of each pixel. The Gabor feature matrix is represented as $X_{\text{Gabor}} \in \mathbb{R}^{N\times D_{\text{Gab}}}$, where D_{Gab} is obtained based on the number of principal components C and the orientations and scales of the Gabor filter. In this article, we employ 40 Gabor filters in 5 scales and 8 orientations and then apply these filters to the top principal component X_{PCA}^1 of the input HSI. Hence, $D_{\text{Gab}} = 5 \times 8 \times 1 = 40$.

B. Constructing ReMass-iForest for Anomaly Detection in the Spatial Domain of HSIs

Given the input HSI data $X \in \mathbb{R}^{N\times D}$, as mentioned earlier, ReMass-iForest applies exactly the same implementation of iTrees as that of iForest [29]. Each iTree is constructed from a small random subsample $X_{\text{sub}} \in \mathbb{R}^{W\times D}$, $(W < N)$, where W denotes pixels randomly selected from the input X. Let X_d denote all the dth band pixels of X_{sub}, and let e denote a randomly selected value between the minimum and maximum of X_d. We recursively divide X_{sub} into two nonempty child nodes by randomly selecting a band d and a split value e, where d is a number between one and D. Specifically, if X_d^w is smaller than e, the wth selected pixel is divided into the left node, and vice versa $(0 < w < W)$. A branch stops splitting when the height of the iTree reaches the height limit $(\log_2 W)$ or the number of pixels in each node equals 1. The iTree construction process is repeated t times, which indicates that the iForest comprises t iTrees.

Here, we give a graphical interpretation for the structure of an iTree as in Fig. 3 inspired by [24]. Each node represents a single pixel or a number of pixels with similar spectral values. Furthermore, we provide details of the construction of ReMass-iForest in Algorithms 1 and 2.

C. Constructing IIF for Anomaly Detection in the Spectral Domain of HSIs

As we have reviewed in Section II, the ReMass-iForest method addresses the problem whereby iForest does not detect local anomalies by using a local ranking measure based on relative mass. The EIF method resolves the poor iForest performance given high-dimensional data by using hyperplanes with random slopes to split data in iTree construction. Because HSI data possess the characteristics of high dimensions and

Algorithm 1 ReMass $-$ iForest(X, t, w)

Input: X - input data, t - number of trees, w - sub-sampling size
Output: a set of t $iTrees$
Initialize $Forest$
set height limit $hl = ceiling\ (\log_2 w)$
for $i = 1$ to t **do**
  $X_{sub} \leftarrow sample(X, w)$
  $Forest \leftarrow Forest \cup iTree(X_{sub}, 0, hl)$
end for
return $Forest$

Algorithm 2 iTree(X, ch, hl)

Input: X - input data, ch - current tree height, hl - height limit
Output: an $iTree$
if $ch \geq hl$ or $|X| \leq 1$ **then**
  return $exNode\{Size \leftarrow |X|\}$
else
  let D be a list of bands of X
  randomly select a band $d \in D$
  randomly select a split value e from max and min values of the dth band of X
  let X_d^i be the value of the ith row and dth column of X
  $X_l \leftarrow filter(X, X_d^i < e)$
  $X_r \leftarrow filter(X, X_d^i \geq e)$
  return $inNode\{Left \leftarrow iTree(X_l, ch+1, hl)$,
    $Right \leftarrow iTree(X_r, ch+1, hl)$,
    $SplitBand \leftarrow d$,
    $SplitValue \leftarrow e\}$
end if

Algorithm 3 Improved $-$ iForest(X, t, w, k)

Input: X - input data, t - number of trees, w - sub-sampling size, k - high-value band subset size
Output: a set of t $iTrees$
Initialize $Forest$
set height limit $hl = ceiling\ (\log_2 w)$
for $i = 1$ to t **do**
  $X_{sub} \leftarrow sample(X, w)$
  $Forest \leftarrow Forest \cup IiTree(X_{sub}, 0, hl, k)$
end for
return $Forest$

Algorithm 4 IiTree(X, ch, hl, k)

Input: X - input data, ch - current tree height, hl - height limit, k - high-value band subset size
Output: an $IiTree$
if $ch \geq hl$ or $|X| \leq 1$ **then**
  return $exNode\{Size \leftarrow |X|\}$
else
  randomly select a normal vector $\vec{n} \in \mathbb{R}^{D\times 1}$ by drawing each coordinate of $\vec{n}$ from a standard Gaussian distribution
  randomly select an intercept vector $\vec{e} \in \mathbb{R}^{1\times D}$ in the range of X
  calculate $sep(X)$ according to (8)
  obtain redundant band subset C_{rb} according to k
  set the coordinates of $\vec{n}$, corresponding to C_{rb}, to zero
  $X_l \leftarrow filter(X, (\vec{x} - \vec{e}) \cdot \vec{n} \leq 0)$
  $X_r \leftarrow filter(X, (\vec{x} - \vec{e}) \cdot \vec{n} > 0)$
  return $inNode\{Left \leftarrow IiTree(X_l, ch+1, hl, k)$,
    $Right \leftarrow IiTree(X_r, ch+1, hl, k)$,
    $Normal \leftarrow \vec{n}$,
    $Intercept \leftarrow \vec{e}\}$
end if

a complex background, iForest-based hyperspectral anomaly detectors face two key challenges: 1) the detection of local anomaly pixels in a complex background; and 2) the selection of more separable bands during iTree construction. Aiming at the first challenge, the proposed IIF algorithm overcomes it by sharing the consideration of relative mass to formulate anomaly scores with ReMass-iForest. Note that the ReMass-iForest and improved-iForest are different in terms of how they construct their iTrees.

Regarding the second challenge, the proposed IIF algorithm selects a subset of bands that contains more discriminative and informative features between the anomaly and background at each branching step in the process of building an iTree. Specifically, let X_d denote all the dth band pixels of HSI data X, and X_d^a and X_d^b denote the anomaly pixels and background pixels, respectively, of X_d, while a threshold td is required to separate all pixels into X_d^a and X_d^b. We propose a separability criterion inspired by [40], which is defined as

$$\operatorname{sep}(X_d) = \frac{\sigma(X_d) - \operatorname{avg}\big(\sigma(X_d^a), \sigma(X_d^b)\big)}{\sigma(X_d)} \tag{8}$$

where $X_d^a \cup X_d^b = X_d$; $\sigma(\cdot)$ is the standard deviation function; and $\operatorname{avg}(x, y)$ simply returns $(x+y)/2$. This criterion is normalized using $\sigma(X_d)$, and in terms of the standard deviation calculation, a reliable one-pass solution with low computational cost can be found in [41]. Obviously, the value of sep$(\cdot)$ is affected by threshold td. However, a proper value of threshold td is difficult to determine when the prior knowledge of anomalies is unknown. To address this problem, the following three steps are employed: 1) generating a series of thresholds in sequence from $\min(X_d)$ to $\max(X_d)$; 2) calculating the corresponding values of separability index sep$(\cdot)$ with (8); and 3) selecting the maximum sep$(\cdot)$. As a result, we obtain a separability index for each band to determine its separability in the identification of background and anomaly pixels. Let sep(X_i) denote the separability index of the ith band, and td_i denote the best corresponding threshold, where $1 < i < D$. Once every band separability index in the given HSI data has been calculated with (8), these separability indexes can be ranked in descending order of their sep$(\cdot)$ value. The bands among the top k of the list are chosen as the high-value band subset, denoted as C_{vb}, whereas the other bands are regarded as the redundant band subset, denoted as C_{rb}. Therefore, for a given D-band HSI, inspired by [31], the branching criterion in

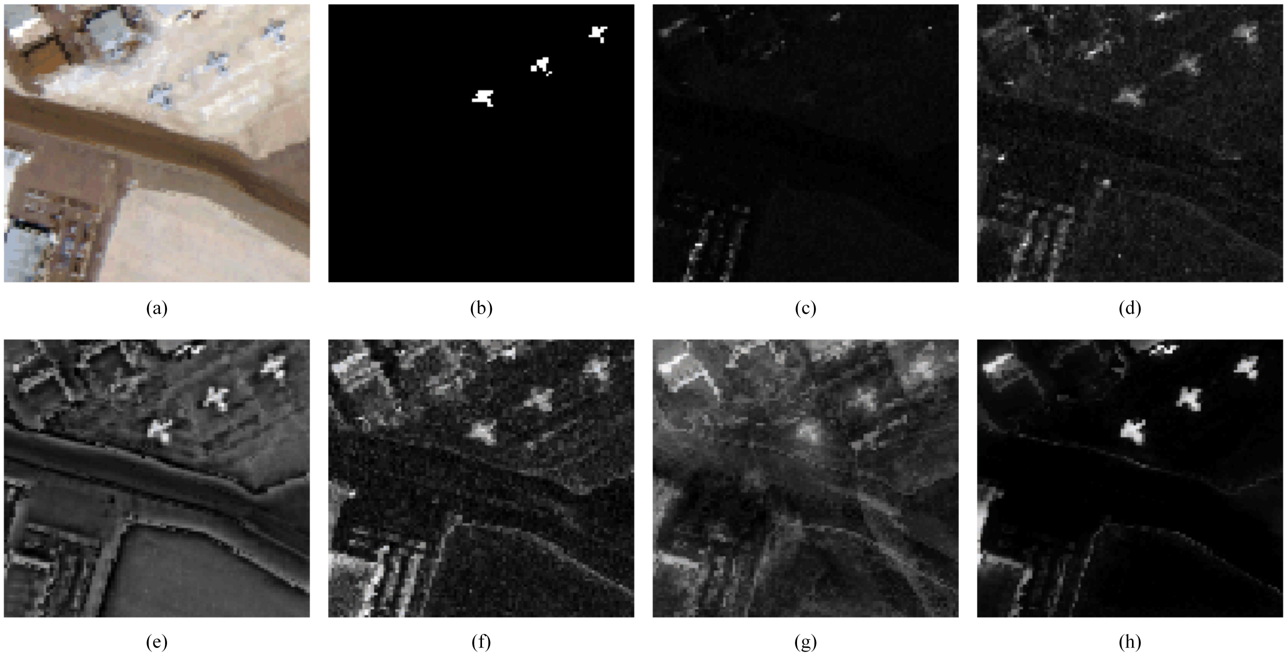

Fig. 4. San Diego-I dataset. (a) Pseudocolor image. (b) Ground-truth map and detection maps of (c) RXD, (d) CRD, (e) PTA, (f) KIFD, (g) MFIFD, and (h) SSIIFD.

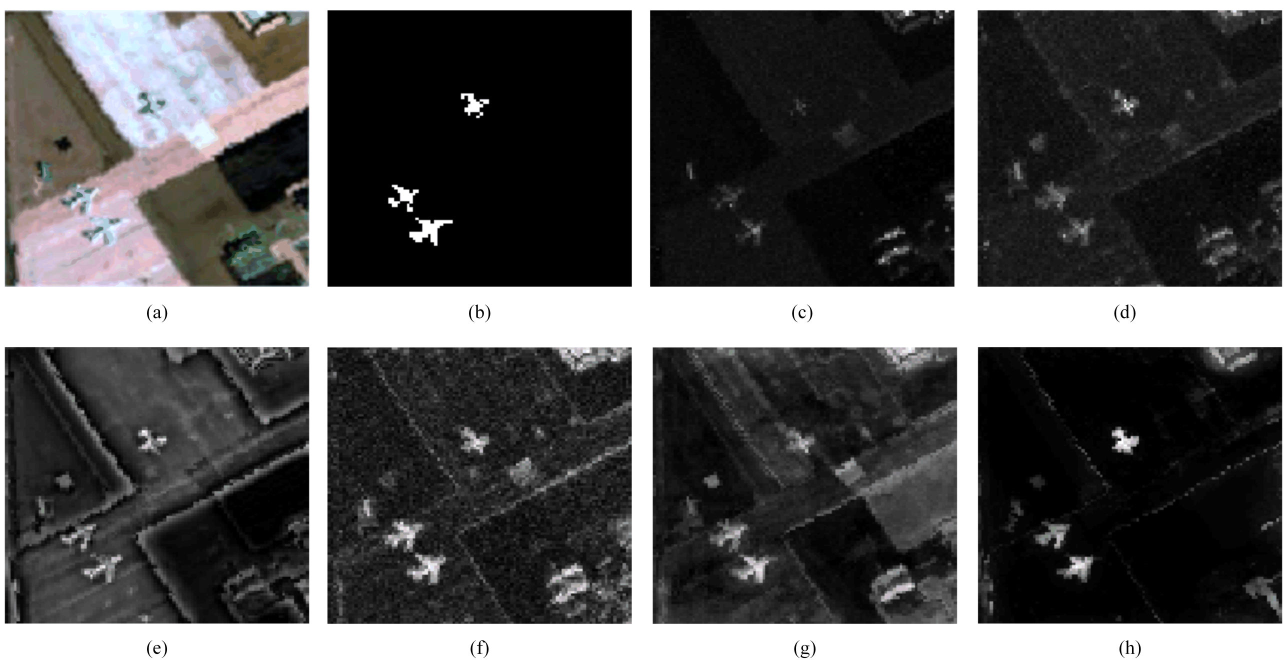

Fig. 5. San Diego-II dataset. (a) Pseudocolor image. (b) Ground-truth map and detection maps of (c) RXD, (d) CRD, (e) PTA, (f) KIFD, (g) MFIFD, and (h) SSIIFD.

terms of data splitting for a given pixel $\boldsymbol{x} = \{x_1, x_2, \ldots, x_D\}$ is as follows:

$$(\boldsymbol{x} - e) \cdot \boldsymbol{n} \le 0 \tag{9}$$

where e denotes a randomly selected value between the minimum and maximum of $\boldsymbol{x}$, and $\boldsymbol{n}$ is a D-dimensional normal vector, which is obtained by drawing a random number for each coordinate of $\boldsymbol{n}$ from the standard normal distribution $N(0, 1)$. Then, the coordinates of $\boldsymbol{n}$, corresponding to C_{rb}, are set to zero, e.g., if the 5th, 9th, and 17th bands are regarded as redundant bands with (8), the 5th, 9th, and 17th component of vector $\boldsymbol{n}$ are set to zero. Furthermore, if the condition is satisfied, pixel $\boldsymbol{x}$ is divided into the left node. Otherwise, it is moved down to the right node. These processes are described in more detail in Algorithms 3 and 4.

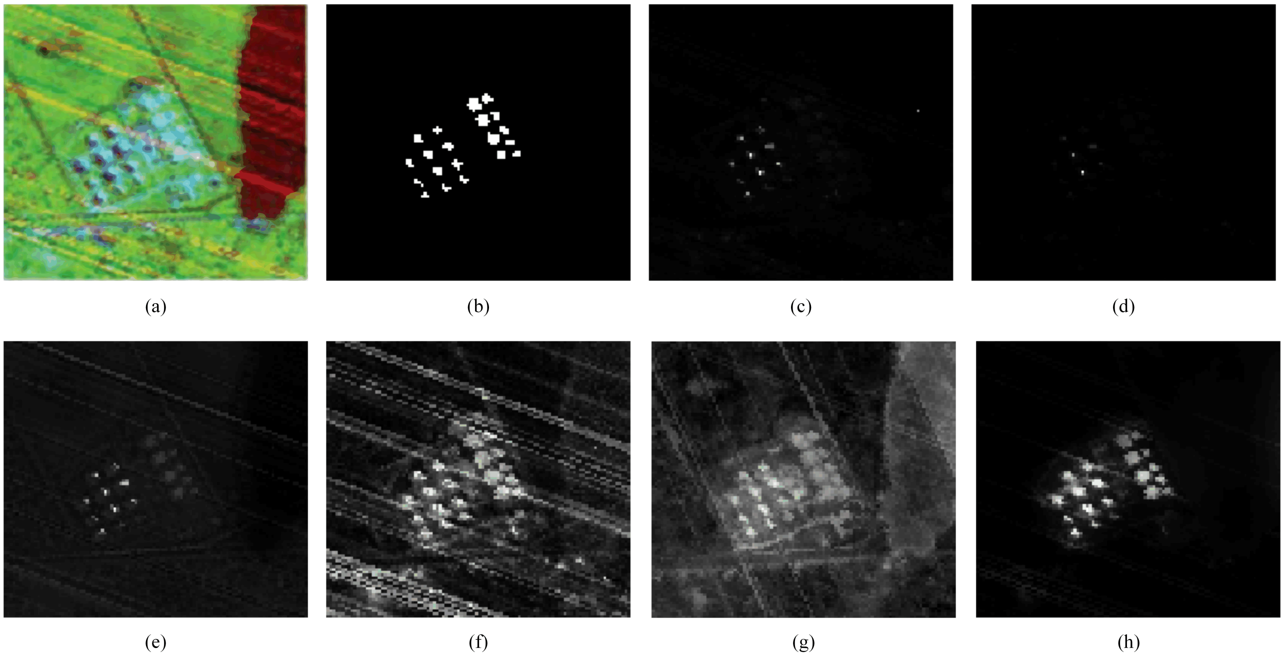

Fig. 6. Texas Coast dataset. (a) Pseudocolor image. (b) Ground-truth map and detection maps of (c) RXD, (d) CRD, (e) PTA, (f) KIFD, (g) MFIFD, and (h) SSIIFD.

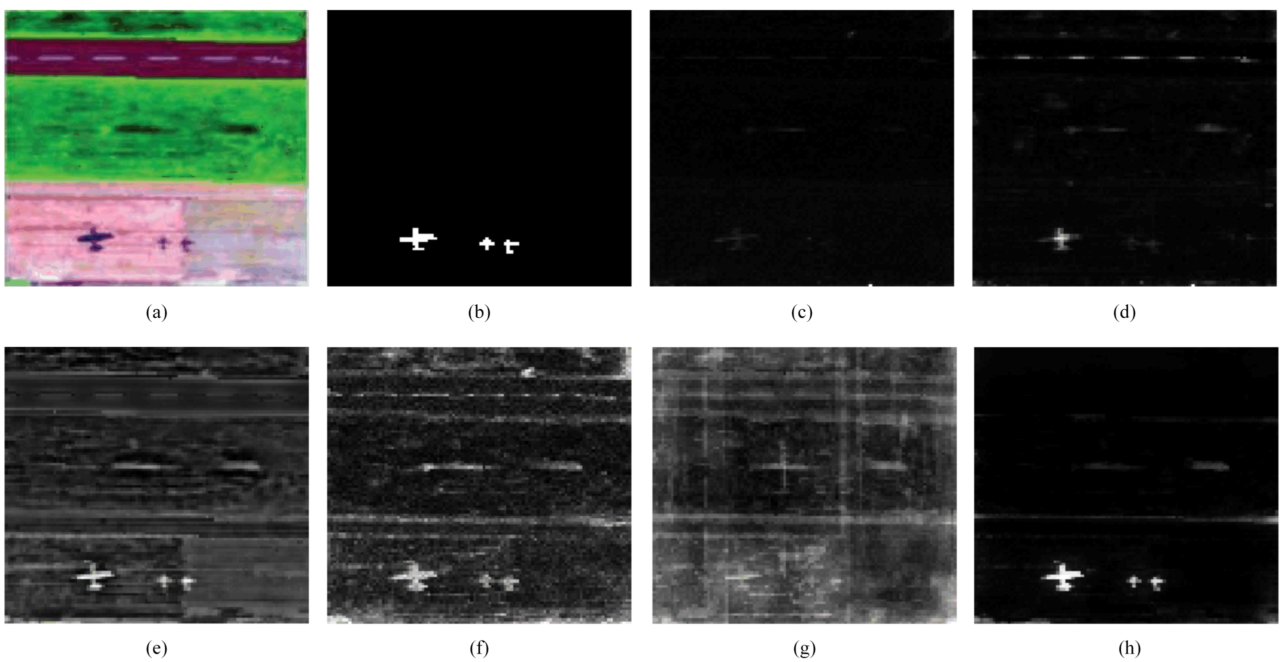

Fig. 7. Gulfport dataset. (a) Pseudocolor image. (b) Ground-truth map and detection maps of (c) RXD, (d) CRD, (e) PTA, (f) KIFD, (g) MFIFD, and (h) SSIIFD.

The proposed IIF method can work directly on the original HSI data. Here, to fully utilize the local information, the original HSI data are segmented into several subregions via the ERS approach before feeding them to the IIF. This preprocessing step exerts a positive influence on fine anomaly detection, which is demonstrated with subsequent experimental results. Specifically, the original data $[X]_{N\times D}$ are transformed into η submatrices: $[^1X]_{N_1\times D}$, $[^2X]_{N_2\times D}$, $\ldots$, $[^\eta X]_{N_\eta\times D}$, where $N_1 + N_2 + \cdots + N_\eta = N$, i.e., $^1X \cup ^2X \cup \cdots \cup ^\eta X = X$.

D. Anomaly Detection Using the Proposed Framework

This section focuses on anomaly detection in both the spatial and spectral domains. As shown in Fig. 1, Gabor features and an HSI marked via ERS are fed to the constructed ReMass-iForest and IIFD, respectively, to detect anomalies. As mentioned earlier, the proposed IIF and ReMass-iForest algorithms share the same measure to detect anomaly pixels, namely both algorithms rely on the relative mass to formulate anomaly scores. In each iTree T_i, the anomaly score of a

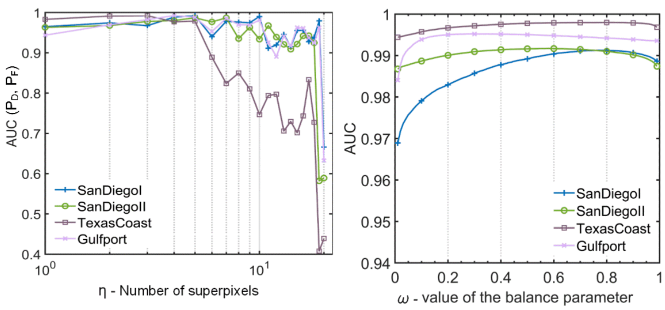

(a) (b)

Fig. 8. Influence of parameters η and ω on the detection performance of the proposed SSIIFD on each HSI dataset. (a) Number of superpixels, η. (b) Value of the balance parameter, ω.

pixel x with respect to its local neighborhood, $s_i(x)$, can be estimated as the ratio of the data mass as follows:

$$s_i(x) = \frac{m\left(\check{T}_i(x)\right)}{m(T_i(x)) \times w} \tag{10}$$

where $T_i(x)$ denotes the leaf node in T_i in which x falls, $\check{T}_i(x)$ denotes the immediate parent of $T_i(x)$, and $m(\cdot)$ denotes the data mass of a tree node. Moreover, w is a normalization term, which is the subsample size used to construct T_i. Obviously, $s_i(\cdot)$ occurs in $(0, 1)$. The higher the score, the higher the likelihood of x being an anomaly pixel. In contrast to the path length in iForest, $s_i(x)$ measures the degree of anomaly locally. Then, the anomaly score $S(x)$ of a test pixel x can be calculated as the average of the local anomaly scores over t iTrees as follows:

$$S(x) = \frac{1}{t}\sum_{i=1}^{t} s_i(x). \tag{11}$$

By carrying out the operations mentioned above for each pixel in the Gabor features and HSI data segmented by ERS, the spatial anomaly score S_{spa} and the spectral anomaly score S_{spe} can be obtained. In order to take full advantage of the spatial and spectral detection results, S_{spa} and S_{spe} are linearly combined to precisely distinguish anomaly pixels from the background as follows:

$$S_0 = \omega S_{\text{spe}} + (1-\omega) S_{\text{spa}} \tag{12}$$

where ω is a balance parameter. As known, the spectral domain in HSI data contains more precise information than the spatial domain. Notably, when the value of ω is greater than 0.5, this suggests that the spectral features play a more important role in the final detection result than the spatial features.

IV. Experiments

In this section, we carry out several experiments to evaluate the detection performance of the proposed SSIIFD method, and comparison results against five state-of-the-art detectors are presented. All experimental algorithms are implemented on a PC with Windows 10, Intel Core i7-9700 CPU@3.00 GHz and 16 GB RAM, and MATLAB 2017b.

A. Hyperspectral Datasets

Here, four real hyperspectral datasets captured at different scenes are employed to evaluate the effectiveness of the proposed SSIIFD method, which are listed as follows:

1) San Diego-I Dataset: The first dataset was captured by the Airborne Visible/Infrared Imaging Spectrometer (AVIRIS) over the airport area of San Diego, CA, USA. The spatial resolution is approximately 3.5 m/pixel, and the spectral resolution is 10 nm. It contains 224 spectral channels in wavelengths ranging from 370 to 2510 nm. After the removal of water absorption and noisy bands (1–6, 33–35, 97, 107–113, 153–166, and 221–224), 189 bands are retained in the experiments. The whole image scene covers an area of 400 × 400 pixels. A region with a size of 100 × 100 pixels is selected from the top left of the image, denoted as San Diego-I. Three airplanes, denoted by 58 pixels, are the anomalies to be detected in this scene. The sample image and ground truth map are shown in Fig. 4(a) and (b), respectively.

2) San Diego-II Dataset: The second dataset has been widely used in related publications [25], [28], [38], and [45]–[49]. Compared to the San Diego-I dataset, this region exhibits a size of 100 × 100 pixels located at the center of the whole image, which is selected for anomaly detection and denoted as San Diego-II. This dataset is an airport scene in which the main background types are hangars, parking aprons, and exposed soil. Three airplanes, denoted by 134 pixels, accounting for 1.34% of the image, are the objects to be detected in this scene. The largest airplane of this dataset obtains 56 pixels and accounts for 0.56% of the image. The sample image and ground-truth map are shown in Fig. 5(a) and (b), respectively.

3) Texas Coast Dataset: The third dataset was captured by the AVIRIS sensor over an urban area of Texas Coast, TX, USA. This urban scene consists of 100 × 100 pixels, with 207 spectral channels in wavelengths ranging from 450 to 1350 nm. The spatial resolution is 17.2 m/pixel. The scene mainly consists of a stretch of meadow and three highways. Houses are regarded as the anomalies in this scene. This HSI is corrupted by serious strip noise, which resulted in challenges in the detection of the above anomaly pixels. The sample image and ground-truth map are shown in Fig. 6(a) and (b), respectively.

4) Gulfport Dataset: The fourth dataset was captured by the AVIRIS over the airport area of Gulfport, MS, USA. This airport scene consists of 100 × 100 pixels, with 191 spectral channels in wavelengths ranging from 550 to 1850 nm. The spatial resolution is 3.4 m/pixel. This scene mainly comprises an airport runway, highway, and some vegetation. Three airplanes of different sizes are the anomalies to be detected. The sample image and ground truth map are shown in Fig. 7(a) and (b), respectively.

B. Comparison Methods and Evaluation Indexes

In our experiments, the anomaly detection performance of the proposed SSIIFD is evaluated and compared to that of five state-of-the-art detectors: RXD [6], CRD [50], PTA [15], KIFD [24], and MFIFD [28]. Specifically, RXD is a representative statistical modeling-based technique. CRD is a typical collaborative representation-based technique. PTA is a typical tensor representation method. The KIFD and MFIFD methods are representative iForest-based techniques. Furthermore, for the CRD, the window sizes and the optimal regularization parameter are set optimally according to the original literature [50], i.e., the inner window size w_{in} (ranging from 3 to 21) and the outer window size w_{out} (ranging from 27 to 41) are selected optimally. The regularization parameter λ_{CRD} is set to 10^{-6}. The PTA parameters are set according to the suggestions in [15], i.e., the truncated low rank r is set to 1 and hyperparameters α, β, μ, and τ are set to 1, 0.01, 0.001, and 1, respectively. In terms of the KIFD method, the subsample size is set to 3% of all pixels in the image, the number of trees $q = 1000$, and the number of principal components $\xi = 300$, which are consistent with the original work [24]. The parameters of MFIFD method are set the same as those given in [28], i.e., the subsample size $\psi = 256$, and the number of trees is set to 25. In summary, the parameters of the five baselines are defined in accordance with the original works [6], [50], [15], [24], [28].

In the experiments, both qualitative and quantitative evaluation approaches are employed to evaluate the detection performance. Specifically, we report the qualitative analysis of the detection performance with the detection map, whereas quantitative evaluation is conducted by using the 3-D receiver operating characteristic (ROC) curve, area under the curve (AUC) values, and separability range. 3-D ROC analysis has recently developed as an effective evaluation approach for target/anomaly detection [52] and classification [53]. The 3-D ROC curve of (P_D, P_F, τ) extends the traditional 2-D ROC curve of detection probability (P_D) and false alarm probability (P_F) by including the threshold τ to specify a third dimension. The P_D and P_F are defined as follows:

$$P_D = \frac{N_D}{N_O} P_F = \frac{N_F}{N} \tag{13}$$

where N_D denotes the number of detected object pixels, N_O denotes the total number of real object pixels, N_F denotes the number of false alarm pixels, and N denotes the total number of pixels in the ROC curve can be employed to generate three 2-D ROC curves, 2-D ROC curve of (P_D, P_F), 2-D ROC curve of (P_D, τ), and 2-D ROC curve of (P_F, τ). The AUC values denoted by AUC (P_D, P_F), AUC (P_D, τ), and AUC (P_F, τ) are calculated from 2-D ROC curve of (P_D, P_F), 2-D ROC curve of (P_D, τ), and 2-D ROC curve of (P_F, τ), respectively. These AUC values can be further used to design two new metrics: AUC_{OD} and AUC_{SNPR} [54]. The AUC_{OD} is used to measure the overall detection performance, which is defined by

$$\text{AUC}_{\text{OD}} = \text{AUC}(P_D, P_F) + \text{AUC}(P_D, \tau) - \text{AUC}(P_F, \tau). \tag{14}$$

The AUC_{SNPR} is called signal-to-noise probability ratio, which originates from a similar idea that is widely used in communications/signal processing, the signal-to-noise ratio (SNR). AUC_{SNPR} is the most effective detection measure, which is defined by

$$\text{AUC}_{\text{SNPR}} = \text{AUC}(P_D, \tau)/\text{AUC}(P_F, \tau). \tag{15}$$

Specifically, a higher value of $\text{AUC}(P_D, P_F)$ and $\text{AUC}(P_D, \tau)$ indicates a better detection performance, while a lower value of $\text{AUC}(P_F, \tau)$ indicates a better background suppression and thus a better detection performance. Naturally, by definition, a better and more effective anomaly detector usually achieves a higher value of AUC_{OD} and AUC_{SNPR}. More details on these metrics have been reported in [52]. Moreover, the separability range clearly describes the ability of a detector to distinguish anomaly pixels from the background [44]. Specifically, a good detector typically features a distinct gap between the anomaly pixels and the background; meanwhile, the anomaly scores of the background are suppressed within a small range.

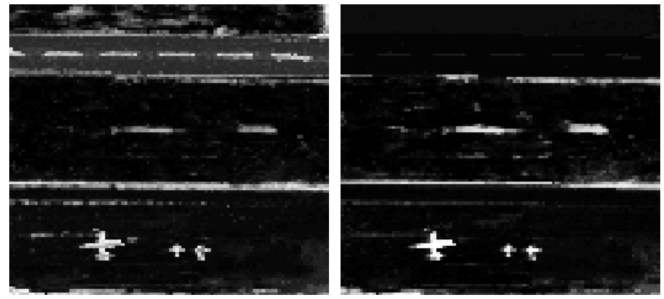

(a) (b)

Fig. 9. Detection map of the proposed IIFD on the Gulfport dataset (a) without pre-segmentation and (b) with ERS algorithm as a preprocessing.

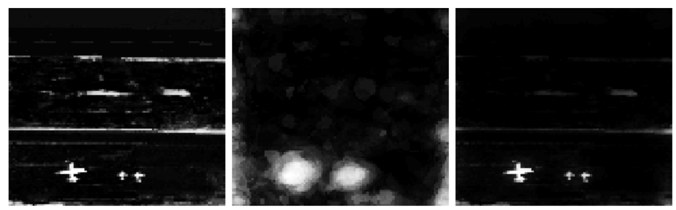

(a) (b) (c)

Fig. 10. Gulfport dataset. (a) Spectral anomaly detection map. (b) Spatial anomaly detection map. (c) Final anomaly detection map.

C. Parameter Tuning

Here, we investigate the influences of the parameters η and ω on the detection performance of the proposed SSIIFD method. Parameter η controls the number of subregions in the preprocessing step. It should be noted that the ERS algorithm addresses the problem that the size of subregions varies greatly under complex background. This occurs mainly because the entropy rate encourages formation of compact and homogeneous clusters, while the balancing function favors clusters with similar sizes. Parameter ω controls the proportion of the spectral anomaly scores in the final detection results. Fig. 8 shows the effect of parameters η and ω on the AUC (P_D, P_F) value of the proposed detector given each dataset.

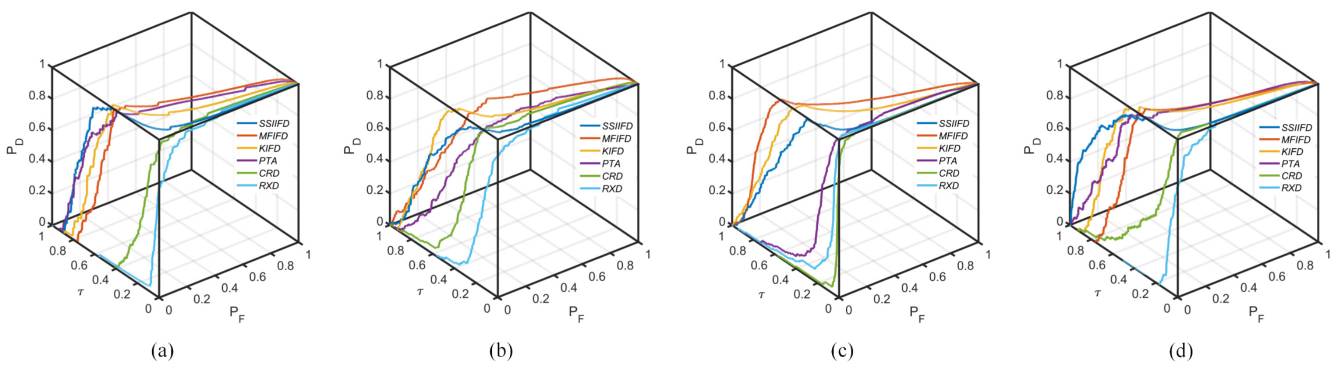

Fig. 11. Three-dimensional ROC curves obtained by the compared methods on (a) San Diego-I, (b) San Diego-II, (c) Texas Coast, and (d) Gulfport datasets.

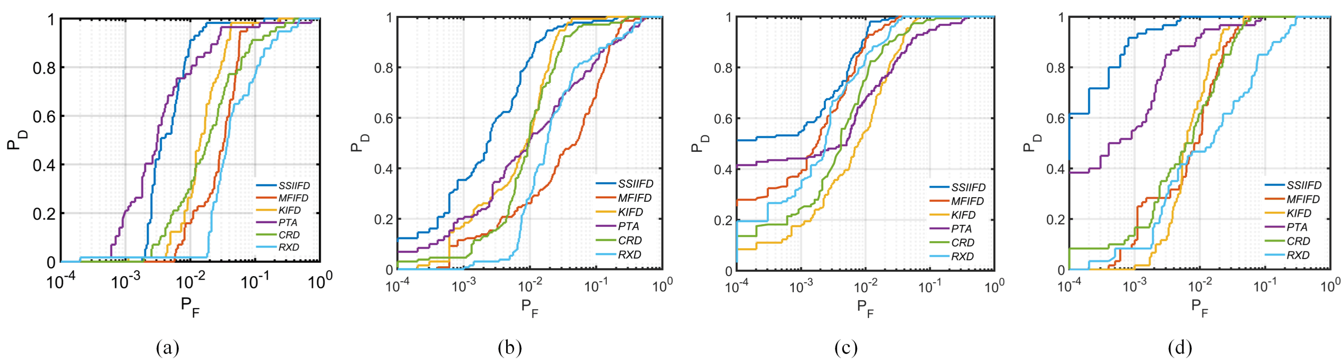

Fig. 12. Normalized 2-D ROC curves of (P_D, P_F) obtained by the compared methods on (a) San Diego-I, (b) San Diego-II, (c) Texas Coast, and (d) Gulfport datasets.

TABLE I

AUC Values of the Methods for the Experimental Datasets

Data Sets	AUC Values	SSIIFD	MFIFD [28]	KIFD [24]	PTA [15]	CRD [50]	RXD [6]
San Diego-I	AUC(P_D, P_F)	0.9924	0.9630	0.9787	0.9792	0.9885	0.9220
	AUC(P_D, τ)	0.7354	0.5988	0.6499	0.7014	0.4465	0.0806
	AUC(P_F, τ)	0.0469	0.2629	0.1640	0.2316	0.1100	0.0398
	AUC_{OD}	**1.6809**	1.2989	1.4646	1.4490	1.3249	0.9628
	AUC_{SNPR}	**15.6748**	2.2777	3.9623	3.0285	4.0594	2.0252
San Diego-II	AUC(P_D, P_F)	0.9916	0.9271	0.9883	0.9406	0.9801	0.9423
	AUC(P_D, τ)	0.6433	0.6759	0.6963	0.5182	0.3587	0.1806
	AUC(P_F, τ)	0.0369	0.3226	0.1529	0.1868	0.1078	0.0589
	AUC_{OD}	**1.5979**	1.2804	1.5317	1.2721	1.2310	1.0639
	AUC_{SNPR}	**17.4173**	2.0952	4.5550	2.7746	3.3281	3.0643
Texas Coast	AUC(P_D, P_F)	0.9972	0.9961	0.9865	0.9769	0.9887	0.9946
	AUC(P_D, τ)	0.6401	0.7155	0.7217	0.2221	0.0355	0.1121
	AUC(P_F, τ)	0.0294	0.2267	0.1582	0.0685	0.0058	0.0135
	AUC_{OD}	**1.6079**	1.4848	1.5501	1.1304	1.0184	1.0931
	AUC_{SNPR}	**21.7566**	3.1561	4.5624	3.2402	6.1036	8.2909
Gulfport	AUC(P_D, P_F)	0.9996	0.9882	0.9904	0.9955	0.9880	0.9526
	AUC(P_D, τ)	0.8114	0.5503	0.6926	0.6900	0.2777	0.0736
	AUC(P_F, τ)	0.0297	0.1902	0.1745	0.1881	0.0299	0.0248
	AUC_{OD}	**1.7813**	1.3483	1.5085	1.4974	1.2359	1.0015
	AUC_{SNPR}	**27.3609**	2.8933	3.9692	3.6675	9.3028	2.9742

Based on the parameter tuning results, we can draw three conclusions, which are listed as follows:

1) The detection performances, represented by AUC (P_D, P_F) values, tend to increase and then decrease with an increasing number of superpixels. This is mainly because excess superpixels will lead to oversegmented regions and cannot fully utilize all samples that belong to the homogeneous area, whereas a small number of superpixels will lead to

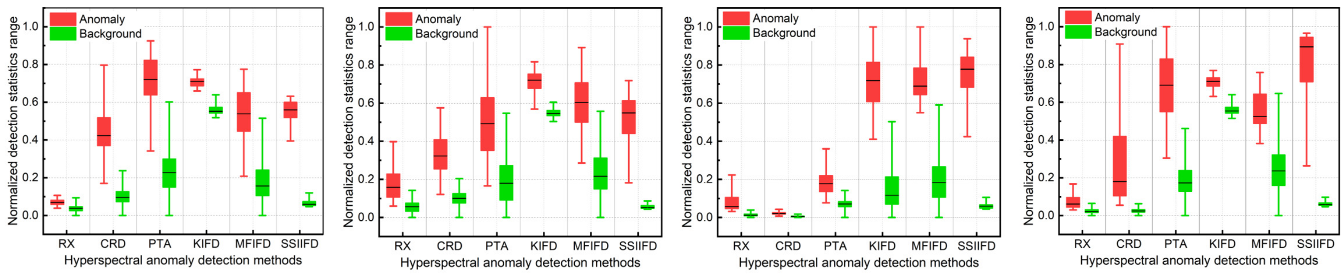

(a) (b) (c) (d)

Fig. 13. Background-anomaly separability maps of the algorithms for (a) San Diego-I dataset, (b) San Diego-II dataset, (c) Texas Coast dataset, and (d) Gulfport dataset.

TABLE II
RUNNING TIME (SECONDS) OF THE METHODS FOR THE EXPERIMENTAL DATASETS

Data Sets	SSIIFD	MFIFD [28]	KIFD [24]	PTA [15]	CRD [50]	RXD [6]
San Diego-I	8.78	2.46	222.27	26.61	941.38	0.16
San Diego-II	8.67	2.54	219.18	24.35	956.98	0.13
Texas Coast	7.12	2.45	222.03	27.17	2077.46	0.11
Gulfport	7.26	2.62	218.91	24.12	379.96	0.14

undersegmentation and introduce some samples from different homogeneous areas and cannot make full use of local information. Moreover, an excessively large number of superpixels results in each region containing a limited number of pixels, which does not guarantee the reliability and stability of the detection results, e.g., all the pixels in a given region may be anomaly pixels, which introduces a high missed detection rate.

2) The detection performance, considering a proper value of η, is always better than that when the η value is set to 1 (which indicates that the proposed method is directly carried out on the original HSI data without preprocessing). Hence, the proposed method, which takes the local homogeneity of HSIs into account, is more effective than the method without segmentation preprocessing.

3) As shown in Fig. 8(b), when parameter ω ranges from 0.01 to 1, the AUC (P_D, P_F) values initially increase, then slightly decrease, and finally reach their peaks at approximately 0.6 for the San Diego-II and Texas Coast datasets. In regard to the San Diego-I and Gulfport datasets, we can observe that maximum AUC (P_D, P_F) values occur at 0.8 and 0.2, respectively.

In summary, based on the experiments and analysis mentioned above, we obtained the optimal fundamental superpixel number η for the Texas Coast, San Diego-II, and the other two datasets at 3, 5, and 4, respectively. Additionally, in this article, we, inspired by [42], set ω to 0.618 for each dataset under the guidance of the golden section method.

D. Analysis of the Detection Performance With and Without Employing the ERS Algorithm

In this section, the influence of the pre-segmentation step on detection performance of the proposed detector IIFD was investigated. Here, the IIFD with segmentation preprocessing by the ERS algorithm is denoted as Local_IIFD, while the IIFD without pre-segmentation is denoted as Global_IIFD. Note that the proposed Local_IIFD is identically equivalent to the proposed Global_IIFD when the superpixel number η is set to 1. As shown in Fig. 7(a), the Gulfport dataset mainly comprises an airport runway, highway, and some vegetation. Three airplanes of different sizes are the anomalies to be detected. However, although the highway is a relatively homogeneous cluster, pixels of the highway, especially the lane line, are easily mistaken for anomalies with global detectors. As shown in Fig. 9(a), the Global_IIFD separates both the airplanes and highway from the background. Conversely, the Local_IIFD segments the Gulfport dataset into four subregions with the ERS algorithm and further detects anomalies on each subregion in turn, which considers both the spectral signature and the spatial information at neighboring locations. As a consequence, some false alarms (e.g., highway pixels) are effectively removed and three airplanes are detected more effectively. The detection map of the Local_IIFD is shown in Fig. 9(b). The AUC (P_D, P_F) score of the detection result is 0.9907.

Based on this experiment, the ERS preprocessing exerts a positive influence on fine anomaly detection.

E. Analysis of the Detection Performance With and Without Employing Spatial Information

In this section, we investigate the influence of spatial information on the detection performance of the proposed method. As shown in Fig. 10(a), the proposed IIFD detects most anomaly pixels in the original Gulfport dataset, and the AUC (P_D, P_F) score of the detection result is 0.9907, from which we can draw two conclusions: 1) the IIFD effectively detects most anomalies without relying on spatial information; and 2) a high false alarm rate (FAR) is the main problem. Therefore, the Gabor filter is applied to extract spatial information in the PCA-projected subspace, and the extracted Gabor features are then employed as input to the ReMass-iForest detector to obtain the spatial anomaly score. The detection map is shown in Fig. 10(b). In addition, the original Gulfport dataset is segmented into four subregions with the ERS approach, and each subregion is fed to the IIFD to obtain the spectral anomaly score in turn. Finally, we fuse the detection results by linearly combining the obtained spatial and spectral anomaly scores to predict the anomaly pixels given the input Gulfport dataset. As such, some false alarms are effectively removed. Fig. 10(c) shows the final detection map and the AUC (P_D, P_F) score of the final detection map is 0.9993.

Based on this experiment, we observe that both spectral and spatial information play an important role in the detection of anomaly pixels.

F. Detection Performance

In this section, we first qualitatively investigate the detection performance via detection maps. For example, in Figs. 4 and 5, the proposed SSIIFD, PTA, KIFD, and MFIFD detect the locations and shapes of the three airplanes accurately. However, PTA, KIFD, and MFIFD also falsely detect many anomalies, whereas there are few false alarms in the detection result obtained with SSIIFD. CRD detects the locations of the three airplanes, but the shapes of these three airplanes are not determined. Additionally, the proposed SSIIFD achieves a robust detection performance in images corrupted by serious strip noise. As shown in Fig. 6, the proposed SSIIFD, KIFD, and MFIFD effectively detect most anomalies, while only SSIIFD effectively removes the interference of strip noise and suppresses most of the background into low-detection outputs. Regarding anomaly targets with relatively irregular and different shapes and sizes, as shown in Fig. 7, CRD fails to detect two small airplanes. MFIFD also fails to detect two small airplanes clearly due to the blurring effect produced in the filtering operation. The PTA and KIFD methods detect all three airplanes, while some background pixels are mistakenly detected as anomalies.

Moreover, the detection performances of the compared methods were quantitatively evaluated based on the AUC scores as summarized in Table I, and the best results are highlighted for each dataset. It is obvious that SSIIFD achieved the best results on all datasets. Although the MFIFD and KIFD methods yielded a relatively stable detection performance, they failed to achieve the highest $\mathrm{AUC}_{\mathrm{OD}}$ or $\mathrm{AUC}_{\mathrm{SNPR}}$ scores in any experiment. Additionally, the 3-D ROC curves and 2-D ROC curves of (P_D, P_F) of the different methods are shown in Figs. 11 and 12, respectively. It can be observed that the SSIIFD method is superior to the MFIFD, KIFD, PTA, CRD, and RXD methods under most conditions.

Furthermore, another quantitative evaluation aspect of the proposed SSIIFD, separability map, is exploited to investigate its ability in anomaly background separation, as shown in Fig. 13. There are two boxes for each detector. The green and red boxes indicate the distributions of the background and anomalies, respectively. The position of the boxes reflects the separability between the background and anomaly pixels. In other words, the greater the distance between these two boxes, the better the detector is. As shown in Fig. 13, it is obvious that the proposed SSIIFD offers the best performance in terms of the separability between the anomalies and background, whereas the other methods exhibit more or less overlap between the anomaly and background boxes. For example, as shown in Fig. 13(b), the proposed SSIIFD, RXD, and CRD effectively suppress the background within a small range. However, for both RXD and CRD, overlap occurs between the anomaly and background boxes, which suggests that they do not efficiently distinguish anomaly pixels from background pixels. On the contrary, the background boxes of PTA and MFIFD reflect that these two methods do not suppress most of the background into low-detection outputs. Based on the experiment results, we conclude that the proposed SSIIFD detects anomaly pixels more clearly and accurately at lower FARs over the five comparison methods.

ReMass-iForest and iForest exhibit the same time complexity, i.e., $\mathrm{O}(t(N+W)\log W)$. The time complexity to construct IIF consists of three major components: 1) computation of the band separability according to (8); 2) sorting of the band separability values; and 3) calculation of the branching criterion according to (8). The time complexity associated with IIF construction of t trees is $\mathrm{O}(tW(DW+\log W+D))$, where W is the subsample size and D is the number of bands in the input HSI. The time complexity of anomaly score evaluation is $\mathrm{O}(tWN)$, where N is the number of pixels in the input HSI. Hence, the time complexity of the proposed IIF is $\mathrm{O}(tW(DW+\log W+D+N))$. Additionally, the compared methods are implemented in MATLAB, and the running times given the four datasets are listed in Table II. It should be noted that RXD is the fastest method, whereas CRD is the slowest. KIFD is also time-consuming, which principally occurs because KIFD employs kernel-PCA during preprocessing, and numerous iTrees are constructed to obtain stable anomaly scores. The running time of the proposed SSIIFD method is similar to that of the MFIFD method, which is much more efficient than the CRD, PTA, and KIFD methods.

G. Sensitivity to the Parameters and Discussion

In this section, we carry out experiments to reveal the effect of the parameters of the proposed SSIIFD method on the detection performance. There are three parameters in the proposed SSIIFD method, i.e., the number of used bands k, the number of iTrees t, and the size of the subsample W. Parameter k controls the number of spectral bands to be employed in the construction of the proposed IIF. Fig. 14 shows the influence of different numbers of iTrees t on the detection performance and the running time on each dataset. As shown in Fig. 14(a), the AUC (P_D, P_F) value for the Gulfport dataset remains nearly stable, whereas the AUC (P_D, P_F) value for the San Diego-II dataset slightly fluctuates within a small range. Regarding the other two datasets, the AUC (P_D, P_F) values initially increase and then fluctuate within a small range. Moreover, as shown in Fig. 14(b), the running time of

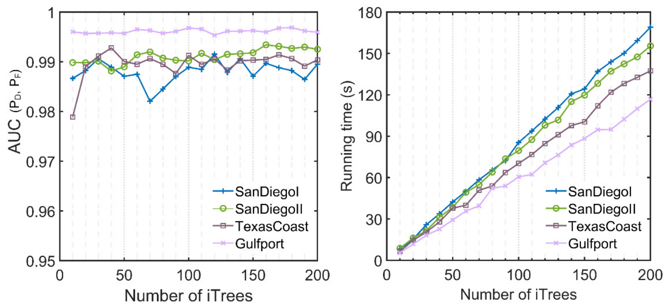

(a) (b)

Fig. 14. Effect of the number of iTrees on each dataset. (a) AUC value. (b) Running time.

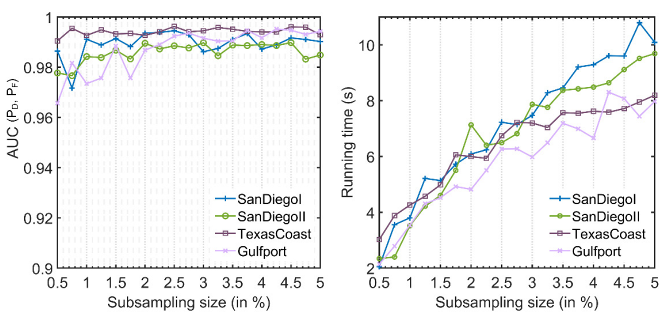

(a) (b)

Fig. 15. Effect of the subsample size on each dataset. (a) AUC value. (b) Running time.

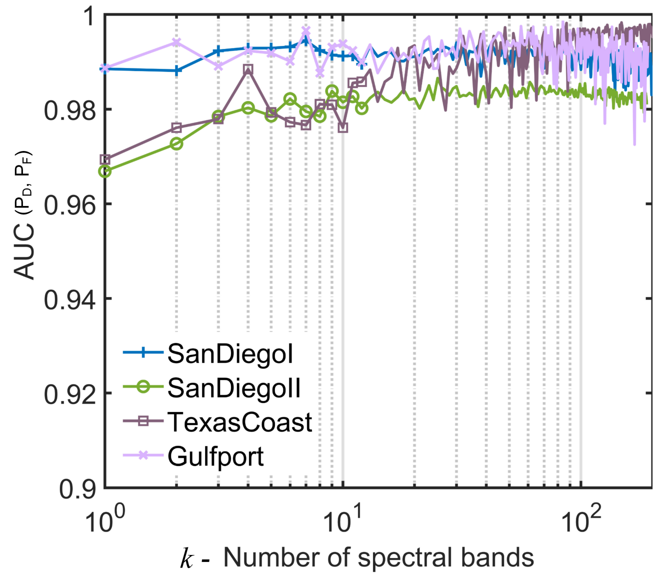

Fig. 16. Influence of the number of used spectral bands k on the detection performance of the proposed SSIIFD on each HSI dataset.

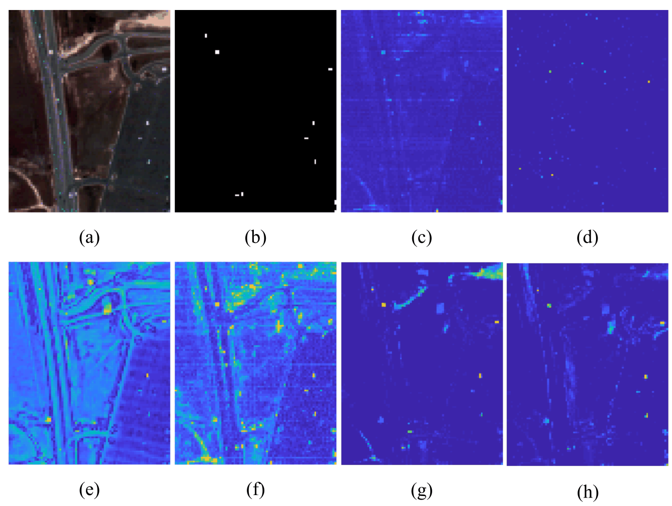

Fig. 17. HYDICE dataset. (a) Pseudocolor image. (b) Ground-truth map and detection maps of (c) RXD, (d) CRD, (e) PTA, (f) KIFD, (g) Global_IIFD, and (h) Local_IIFD.

the proposed SSIIFD method achieves a nearly linear growth with increasing number of iTrees. In addition, Fig. 15 shows the influence of different subsample sizes W on the detection performance and running time on each dataset. As shown in Fig. 15(a), the AUC (P_D, P_F) value for the Texas Coast dataset remains nearly stable, whereas the AUC (P_D, P_F) values for the other three datasets slightly fluctuate within a small range, i.e., from 0.96 to1. Furthermore, as shown in Fig. 15(b), the running time of the proposed SSIIFD method achieves a nearly linear growth with increasing subsample size W. Hence, considering both the performance and efficiency of the proposed SSIIFD method, we set $t = 32$ and $W = \text{ceiling}(2.5\% \times N)$ (where N is the number of pixels in the input HSI) for each dataset as default parameter values.

Moreover, Fig. 16 shows the effect of parameter k on the detection performance given each dataset. Regarding the San Diego-I and San Diego-II datasets, the AUC (P_D, P_F) values gradually increase and tend to remain stable when the parameter k ranges from 1 to 100. On the contrary, the AUC (P_D, P_F) values obtained for the Gulfport and Texas Coast datasets exhibit a larger fluctuation with increasing k. This mainly occurs because pretreatment of water absorption and noisy bands is applied to the two San Diego datasets, and almost all 189 bands exhibit a high SNR, whereas the Gulfport and Texas Coast datasets, without pretreatment, exhibit low SNR and poor quality bands, especially the Texas Coast dataset. As a result, in terms of the two San Diego datasets, by calculating the sep value for each band with (8), we obtain the separability index as expected, which accurately measures how separable each band is in the identification of background and anomaly pixels. For the other two datasets with no pretreatment, too large or too small value of k leads to the usage of those noisy and water absorption-affected bands with a high probability. In other words, in low SNR and noisy bands, the sep value does not accurately measure how separable the band is in distinguishing anomaly pixels from the background. Therefore, parameter k is set as $k = \text{ceiling}(D/3)$ for each dataset in this article.

H. Application of the Proposed Method on Subpixel Target Detection in HSIs

The proposed SSIIFD, a spectral–spatial IIF-based detection framework, is designed to detect anomaly pixels by combining

TABLE III
AUC VALUES OF THE METHODS FOR THE HYDICE DATASET

AUC Values	Local_IIFD	Global_IIFD	KIFD [24]	PTA [15]	CRD [50]	RXD [6]
AUC(P_D, P_F)	0.9952	0.9902	0.9951	0.9869	0.9705	0.9843
AUC(P_D, τ)	0.5687	0.5464	0.8456	0.4539	0.0189	0.2373
AUC(P_F, τ)	0.0157	0.0169	0.2013	0.2259	0.0054	0.0344
AUC_{OD}	1.5482	1.5198	**1.6395**	1.0528	0.9840	1.1872
AUC_{SNPR}	**36.1733**	32.4100	4.2018	2.0093	3.4808	6.9069

spectral and spatial information. To verify the performance of all aspects of the proposed method, previous experiments used four datasets in which spatial information could provide useful information for anomaly detection. Those four datasets are representative of anomalies at full-size pixels. In practice, a small-sized ground target may occupy part of the pixel area and form a mixed pixel with the background of a ground object. In such cases, the corresponding target/anomaly detection problem becomes a subpixel target detection problem.

This section uses the HYperspectral Digital Imagery Collection Experiment (HYDICE) urban dataset to further analyze the detection performance of the proposed detectors on subpixel target detection. The HYDICE urban dataset, available on the website,[2] is representative of anomalies at subpixel level [49]. It was recorded by the HYDICE in October 1995, whose location is an urban area at Copperas Cove, TX, USA. Each pixel, corresponding to a 2 m $\times$ 2 m area, is observed at 162 wavelengths ranging from 440 to 2370 nm after removing the noisy and water vapor absorption bands [51]. A region with a size of 80 $\times$ 100 pixels located at the top right of the scene is selected as the test data. Among them, 21 pixels are identified as anomalies, which are mainly cars, because they have spectra that differ from the background. The sample image and ground-truth map are shown in Fig. 17(a) and (b), respectively.

In subpixel target detection, the size of the target is smaller than that of a pixel, making the spatial information of the target almost useless so that a detector must rely on the spectral information of the image. Hence, rather than the proposed SSIIFD, the proposed Local_IIFD and Global_IIFD are employed to detect the 21 pixels. It should be noted that the proposed SSIIFD is identically equivalent to the proposed Local_IIFD when the parameter ω in (12) is equal to 1. For Local_IIFD, the superpixel number η is set to 3. Other parameter settings are consistent with Sections IV-B and IV-E.

For the HYDICE dataset, the detection maps of the proposed detectors, Local_IIFD, Global_IIFD, and four comparison detectors, are shown in Fig. 17. Their AUC values are listed in Table III. From Fig. 17, it is obvious that both Local_IIFD and Global_IIFD work effectively. Table III tabulates the AUC values of their corresponding 2-D ROC curves, AUC_{OD}, and AUC_{SNPR}, where the best results are boldfaced. Among the best cases is $AUC_{SNPR} = 36.1733$ produced by Local_IIFD. The KIFD produces a very high AUC $(P_D,\ P_F)$ value at the expense of high AUC $(P_F,\ \tau)$, which means that KIFD performs poorly in background suppression, while the proposed Local_IIFD and Global_IIFD show competitive performances for anomaly detection in terms of both detection accuracy and background suppression.

[2]http://www.tec.army.mil/Hypercube

V. CONCLUSION

In this article, we propose a novel IIF algorithm to address the poor performance of iForest in regard to high-dimensional data and detecting local anomalies. Then, a novel spectral–spatial anomaly detection framework based on IIF (SSIIFD) is proposed. Gabor features and segmented HSI data are employed to construct ReMass-iForest and IIF, respectively. The advantages of the proposed SSIIFD method are threefold: 1) the method fully utilizes spectral and spatial information in HSIs; 2) this method fully employs global and local information in HSIs; and 3) this method detects anomaly pixels more clearly and accurately at a lower FAR. The experiments on four real hyperspectral datasets reveal that SSIIFD is stable and superior to other state-of-the-art methods in terms of both objective and subjective evaluations. In the future, the application of SSIIFD in other remote sensing applications will be investigated (e.g., change detection and shadow detection). In addition, how to classify and recognize the detected anomaly pixels will be the focus of our future research.

ACKNOWLEDGMENT

The authors acknowledge Prof. Wei Li for providing the prior-based tensor approximation detector (PTA) codes on his homepage; Dr. Stefania Matteoli and Dr. Xudong Kang for sharing the hyperspectral datasets; and Dr. Rong Wang for the valuable support provided during the programming of the multiple feature and Isolation Forest-based detector (MFIFD). They would also like to thank the editors and anonymous reviewers for their insightful comments and suggestions, which have significantly improved this article.

REFERENCES

[1] G. Shaw and D. Manolakis, "Signal processing for hyperspectral image exploitation," *IEEE Signal Process. Mag.*, vol. 19, no. 1, pp. 12–16, Jan. 2002, doi: 10.1109/79.974715.

[2] D. W. J. Stein, S. G. Beaven, L. E. Hoff, E. M. Winter, A. P. Schaum, and A. D. Stocker, "Anomaly detection from hyperspectral imagery," *IEEE Signal Process. Mag.*, vol. 19, no. 1, pp. 58–69, Jan. 2002, doi: 10.1109/79.974730.

[3] S. Matteoli, M. Diani, and J. Theiler, "An overview of background modeling for detection of targets and anomalies in hyperspectral remotely sensed imagery," *IEEE J. Sel. Topics Appl. Earth Observ. Remote Sens.*, vol. 7, no. 6, pp. 2317–2336, Jul. 2014, doi: 10.1109/JSTARS.2014.2315772.

[4] C.-I. Chang and S.-S. Chiang, "Anomaly detection and classification for hyperspectral imagery," *IEEE Trans. Geosci. Remote Sens.*, vol. 40, no. 6, pp. 1314–1325, Jun. 2002, doi: 10.1109/TGRS.2002.800280.

[5] S. Liu, D. Marinelli, L. Bruzzone, and F. Bovolo, "A review of change detection in multitemporal hyperspectral images: Current techniques, applications, and challenges," *IEEE Geosci. Remote Sens. Mag.*, vol. 7, no. 2, pp. 140–158, Jun. 2019, doi: 10.1109/MGRS.2019.2898520.

[6] I. S. Reed and X. Yu, "Adaptive multiple-band CFAR detection of an optical pattern with unknown spectral distribution," *IEEE Trans. Acoust., Speech Signal Process.*, vol. 38, no. 10, pp. 1760–1770, Oct. 1990, doi: 10.1109/29.60107.

[7] H. Kwon and N. M. Nasrabadi, "Kernel RX-algorithm: A nonlinear anomaly detector for hyperspectral imagery," *IEEE Trans. Geosci. Remote Sens.*, vol. 43, no. 2, pp. 388–397, Feb. 2005, doi: 10.1109/TGRS.2004.841487.

[8] M. J. Carlotto, "A cluster-based approach for detecting man-made objects and changes in imagery," *IEEE Trans. Geosci. Remote Sens.*, vol. 43, no. 2, pp. 374–387, Feb. 2005, doi: 10.1109/TGRS.2004.841481.

[9] J. M. Molero, E. M. Garzón, I. García, and A. Plaza, "Analysis and optimizations of global and local versions of the RX algorithm for anomaly detection in hyperspectral data," *IEEE J. Sel. Topics Appl. Earth Observ. Remote Sens.*, vol. 6, no. 2, pp. 801–814, Apr. 2013, doi: 10.1109/JSTARS.2013.2238609.

[10] W. M. Liu and C. I. Chang, "Multiple-window anomaly detection for hyperspectral imagery," *IEEE J. Sel. Topics Appl. Earth Observ. Remote Sens.*, vol. 6, no. 2, pp. 644–658, Apr. 2013, doi: 10.1109/JSTARS.2013.2239959.

[11] Q. Guo, B. Zhang, Q. Ran, L. Gao, J. Li, and A. Plaza, "Weighted-RXD and linear filter-based RXD: Improving background statistics estimation for anomaly detection in hyperspectral imagery," *IEEE J. Sel. Topics Appl. Earth Observ. Remote Sens.*, vol. 7, no. 6, pp. 2351–2366, Jun. 2014, doi: 10.1109/JSTARS.2014.2302446.

[12] J. Zhou, C. Kwan, B. Ayhan, and M. T. Eismann, "A novel cluster kernel RX algorithm for anomaly and change detection using hyperspectral images," *IEEE Trans. Geosci. Remote Sens.*, vol. 54, no. 11, pp. 6497–6504, Nov. 2016, doi: 10.1109/TGRS.2016.2585495.

[13] Y. Xu, Z. Wu, J. Li, A. Plaza, and Z. Wei, "Anomaly detection in hyperspectral images based on low-rank and sparse representation," *IEEE Trans. Geosci. Remote Sens.*, vol. 54, no. 4, pp. 1990–2000, Apr. 2016, doi: 10.1109/TGRS.2015.2493201.

[14] J. Li, H. Zhang, L. Zhang, and L. Ma, "Hyperspectral anomaly detection by the use of background joint sparse representation," *IEEE J. Sel. Topics Appl. Earth Observ. Remote Sens.*, vol. 8, no. 6, pp. 2523–2533, Jun. 2015, doi: 10.1109/JSTARS.2015.2437073.

[15] L. Li, W. Li, Y. Qu, C. Zhao, R. Tao, and Q. Du, "Prior-based tensor approximation for anomaly detection in hyperspectral imagery," *IEEE Trans. Neural Netw. Learn. Syst.*, early access, Dec. 9, 2021, doi: 10.1109/TNNLS.2020.3038659.

[16] A. Banerjee, P. Burlina, and C. Diehl, "A support vector method for anomaly detection in hyperspectral imagery," *IEEE Trans. Geosci. Remote Sens.*, vol. 44, no. 8, pp. 2282–2291, Aug. 2006, doi: 10.1109/TGRS.2006.873019.

[17] W. Sakla, A. Chan, J. Ji, and A. Sakla, "An SVDD-based algorithm for target detection in hyperspectral imagery," *IEEE Geosci. Remote Sens. Lett.*, vol. 8, no. 2, pp. 384–388, Mar. 2011, doi: 10.1109/LGRS.2010.2078795.

[18] S. Li, K. Zhang, Q. Hao, P. Duan, and X. Kang, "Hyperspectral anomaly detection with multiscale attribute and edge-preserving filters," *IEEE Geosci. Remote Sens. Lett.*, vol. 15, no. 10, pp. 1605–1609, Oct. 2018, doi: 10.1109/LGRS.2018.2853705.

[19] A. Taghipour and H. Ghassemian, "Hyperspectral anomaly detection using attribute profiles," *IEEE Geosci. Remote Sens. Lett.*, vol. 14, no. 7, pp. 1136–1140, Jul. 2017, doi: 10.1109/LGRS.2017.2700329.

[20] W. Li, G. Wu, and Q. Du, "Transferred deep learning for hyperspectral target detection," in *Proc. IEEE Int. Geosci. Remote Sens. Symp. (IGARSS)*, Fort Worth, TX, USA, Jul. 2017, pp. 5177–5180, doi: 10.1109/IGARSS.2017.8128168.

[21] C. Zhao, X. Li, and H. Zhu, "Hyperspectral anomaly detection based on stacked denoising autoencoders," *J. Appl. Remote Sens.*, vol. 11, no. 4, p. 1, Sep. 2017.

[22] N. Ma, Y. Peng, S. Wang, and P. H. W. Leong, "An unsupervised deep hyperspectral anomaly detector," *Sensors*, vol. 18, no. 3, p. 693, Feb. 2018.

[23] S. Song, H. Zhou, Y. Yang, and J. Song, "Hyperspectral anomaly detection via convolutional neural network and low rank with density-based clustering," *IEEE J. Sel. Topics Appl. Earth Observ. Remote Sens.*, vol. 12, no. 9, pp. 3637–3649, Sep. 2019, doi: 10.1109/JSTARS.2019.2926130.

[24] S. Li, K. Zhang, P. Duan, and X. Kang, "Hyperspectral anomaly detection with kernel isolation forest," *IEEE Trans. Geosci. Remote Sens.*, vol. 58, no. 1, pp. 319–329, Jan. 2020.

[25] K. Zhang, X. Kang, and S. Li, "Isolation forest for anomaly detection in hyperspectral images," in *Proc. IEEE Int. Geosci. Remote Sens. Symp. (IGARSS)*, Yokohama, Japan, Jul. 2019, pp. 437–440, doi: 10.1109/IGARSS.2019.8899812.

[26] F. T. Liu, K. M. Ting, and Z.-H. Zhou, "Isolation forest," in *Proc. 8th IEEE Int. Conf. Data Mining*, Dec. 2008, pp. 413–422.

[27] F. T. Liu, K. M. Ting, and Z. Zhou, "Isolation-based anomaly detection," *ACM Trans. Knowl. Discovery Data*, vol. 6, no. 1, pp. 1–39, Mar. 2012.

[28] R. Wang, F. Nie, Z. Wang, F. He, and X. Li, "Multiple features and isolation forest-based fast anomaly detector for hyperspectral imagery," *IEEE Trans. Geosci. Remote Sens.*, vol. 58, no. 9, pp. 6664–6676, Sep. 2020, doi: 10.1109/TGRS.2020.2978491.

[29] S. Aryal, K. M. Ting, J. R. Wells, and T. Washio, "Improving iForest with relative mass," in *Proc. 18th Pacic-Asia Conf. Knowl. Discovery Data Mining (PAKDD)*, 2014, pp. 510–521.

[30] K. M. Ting, G. T. Zhou, F. T. Liu, and S. C. Tan, "Mass estimation," *Mach. Learn.*, vol. 90, no. 1, pp. 127–160, Jan. 2013.

[31] S. Hariri, M. C. Kind, and R. J. Brunner, "Extended isolation forest," *IEEE Trans. Knowl. Data Eng.*, vol. 33, no. 4, pp. 1479–1489, Apr. 2021, doi: 10.1109/TKDE.2019.2947676.

[32] J. G. Daugman, "Uncertainty relation for resolution in space, spatial frequency, and orientation optimized by two-dimensional visual cortical filters," *J. Opt. Soc. Amer. A, Opt. Image Sci.*, vol. 2, no. 7, pp. 1160–1169, Jul. 1985.

[33] D. A. Clausi and M. E. Jernigan, "Designing Gabor filters for optimal texture separability," *Pattern Recognit.*, vol. 33, no. 11, pp. 1835–1849, Nov. 2000.

[34] L. Zhang, L. Zhang, D. Tao, and X. Huang, "On combining multiple features for hyperspectral remote sensing image classification," *IEEE Trans. Geosci. Remote Sens.*, vol. 50, no. 3, pp. 879–893, Mar. 2012.

[35] K.-K. Huang, C.-X. Ren, H. Liu, Z.-R. Lai, Y.-F. Yu, and D.-Q. Dai, "Hyperspectral image classification via discriminant Gabor ensemble filter," *IEEE Trans. Cybern.*, early access, Feb. 5, 2021, doi: 10.1109/TCYB.2021.3051141.

[36] M.-Y. Liu, O. Tuzel, S. Ramalingam, and R. Chellappa, "Entropy rate superpixel segmentation," in *Proc. CVPR*, Jun. 2011, pp. 2097–2104, doi: 10.1109/CVPR.2011.5995323.

[37] G. L. Nemhauser, L. A. Wolsey, and M. L. Fisher, "An analysis of approximations for maximizing submodular set functions-I," *Math. Programm.*, vol. 14, no. 1, pp. 265–294, 1978, doi: 10.1007/BF01588971.

[38] J. Lei, W. Xie, J. Yang, Y. Li, and C.-I. Chang, "Spectral–spatial feature extraction for hyperspectral anomaly detection," *IEEE Trans. Geosci. Remote Sens.*, vol. 57, no. 10, pp. 8131–8143, Oct. 2019, doi: 10.1109/TGRS.2019.2918387.

[39] D. Tao, X. Li, X. Wu, and S. J. Maybank, "General tensor discriminant analysis and Gabor features for gait recognition," *IEEE Trans. Pattern Anal. Mach. Intell.*, vol. 29, no. 10, pp. 1700–1715, Oct. 2007, doi: 10.1109/TPAMI.2007.1096.

[40] T. L. Fei, M. T. Kai, and Z. H. Zhou, "On detecting clustered anomalies using SCiForest," in *Proc. Mach. Learn. Knowl. Discovery Databases, Eur. Conf. (ECML PKDD)*. Barcelona, Spain: Springer-Verlag, Sep. 2010.

[41] D. E. Knuth, *The Art of Computer Programming*, vol. 2, 3rd ed. Reading, MA, USA: Addison-Wesley, 1998, p. 232.

[42] A. P. Stakhov, "The generalized principle of the golden section and its applications in mathematics, science, and engineering," *Chaos, Solitons Fractals*, vol. 26, no. 2, pp. 263–289, Oct. 2005.

[43] T. Fawcett, "An introduction to ROC analysis," *Pattern Recognit. Lett.*, vol. 27, no. 8, pp. 861–874, Jun. 2006.

[44] D. Manolakis and G. S. Shaw, "Detection algorithms for hyperspectral imaging applications," *IEEE Signal Process. Mag.*, vol. 19, no. 1, pp. 29–43, Jan. 2002.

[45] T. Jiang, W. Xie, Y. Li, J. Lei, and Q. Du, "Weakly supervised discriminative learning with spectral constrained generative adversarial network for hyperspectral anomaly detection," *IEEE Trans. Neural Netw. Learn. Syst.*, early access, May 31, 2021, doi: 10.1109/TNNLS.2021.3082158.

[46] K. Jiang *et al.*, "E2E-LIADE: End-to-end local invariant autoencoding density estimation model for anomaly target detection in hyperspectral image," *IEEE Trans. Cybern.*, early access, Jun. 2, 2021, doi: 10.1109/TCYB.2021.3079247.

[47] W. Xie, X. Zhang, Y. Li, J. Lei, J. Li, and Q. Du, "Weakly supervised low-rank representation for hyperspectral anomaly detection," *IEEE Trans. Cybern.*, vol. 51, no. 8, pp. 3889–3900, Aug. 2021, doi: 10.1109/TCYB.2021.3065070.

[48] J. Liu, Z. Hou, W. Li, R. Tao, D. Orlando, and H. Li, "Multipixel anomaly detection with unknown patterns for hyperspectral imagery," *IEEE Trans. Neural Netw. Learn. Syst.*, early access, Apr. 14, 2021, doi: 10.1109/TNNLS.2021.3071026.

[49] W. Xie, Y. Li, J. Lei, J. Yang, C.-I. Chang, and Z. Li, "Hyperspectral band selection for spectral–spatial anomaly detection," *IEEE Trans. Geosci. Remote Sens.*, vol. 58, no. 5, pp. 3426–3436, May 2020, doi: 10.1109/TGRS.2019.2956159.

[50] L. Wei and D. Qian, "Collaborative representation for hyperspectral anomaly detection," *IEEE Trans. Geosci. Remote Sens.*, vol. 53, no. 3, pp. 1463–1474, Mar. 2015, doi: 10.1109/TGRS.2014.2343955.

[51] F. Zhu, Y. Wang, S. Xiang, B. Fan, and C. Pan, "Structured sparse method for hyperspectral unmixing," *ISPRS J. Photogramm. Remote Sens.*, vol. 88, pp. 101–118, Feb. 2014, doi: 10.1016/j.isprsjprs.2013.11.014.

[52] C.-I. Chang, "An effective evaluation tool for hyperspectral target detection: 3D receiver operating characteristic curve analysis," *IEEE Trans. Geosci. Remote Sens.*, vol. 59, no. 6, pp. 5131–5153, Jun. 2021, doi: 10.1109/TGRS.2020.3021671.

[53] M. Song, X. Shang, and C.-I. Chang, "3-D receiver operating characteristic analysis for hyperspectral image classification," *IEEE Trans. Geosci. Remote Sens.*, vol. 58, no. 11, pp. 8093–8115, Nov. 2020, doi: 10.1109/TGRS.2020.2987137.

[54] C.-I. Chang, H. Cao, and M. Song, "Orthogonal subspace projection target detector for hyperspectral anomaly detection," *IEEE J. Sel. Topics Appl. Earth Observ. Remote Sens.*, vol. 14, pp. 4915–4932, Mar. 2021, doi: 10.1109/JSTARS.2021.3068983.

[55] C.-I. Chang, H. Cao, S. Chen, X. Shang, C. Yu, and M. Song, "Orthogonal subspace projection-based go-decomposition approach to finding low-rank and sparsity matrices for hyperspectral anomaly detection," *IEEE Trans. Geosci. Remote Sens.*, vol. 59, no. 3, pp. 2403–2429, Mar. 2021, doi: 10.1109/TGRS.2020.3002724.

[56] Z. Huang, X. Kang, S. Li, and Q. Hao, "Game theory-based hyperspectral anomaly detection," *IEEE Trans. Geosci. Remote Sens.*, vol. 58, no. 4, pp. 2965–2976, Apr. 2020, doi: 10.1109/TGRS.2019.2958359.

Xiangyu Song received the B.S. degree from Shandong University of Technology, Zibo, China, in 2017. He is currently pursuing the joint Ph.D. degree with Changchun Institute of Optics, Fine Mechanics and Physics, Chinese Academy of Sciences, Changchun, China, and the University of Chinese Academy of Sciences, Beijing, China.

His research interests include hyperspectral image classification, anomaly detection, and machine learning.

Sunil Aryal (Member, IEEE) received the Ph.D. degree from Monash University, Melbourne, VIC, Australia, in 2017.

Before moving to academia, he worked in the industry as a Data Engineer and a Software Developer for several years. Prior to joining Deakin University, Burwood, VIC, Australia, in 2019, he worked as a Lecturer with Federation University Australia, Ballarat, VIC, Australia, and Sessional Teaching Staff with various institutions in Australia. He is a Lecturer in the School of Information Technology, Faculty of Science, Engineering and Built Environment, Deakin University. He has been a named investigator on research grants and contracts of over AUD 1.9 million. He has authored more than 30 scientific articles in top tier conferences and journals in the field of data mining and machine learning. His research is in the areas of data mining, machine learning, and artificial intelligence, and their applications to solve real-world problems in defense, healthcare, cybersecurity, and IoT. He works in similarity measures, anomaly detection, classification, clustering, text/image analysis, ensemble learning, learning from small subsamples of data, and robust/explainable machine learning.

Kai Ming Ting received the Ph.D. degree from the University of Sydney, Sydney, NSW, Australia, in 1996.

He worked with the University of Waikato, Hamilton, New Zealand; Deakin University, Burwood, VIC, Australia; Monash University, Melbourne, VIC, Australia; and Federation University Australia, Ballarat, VIC, Australia. He joined Nanjing University, Nanjing, China, in 2020. Research grants received include those from the National Natural Science Foundation of China, U.S. Air Force of Scientific Research (AFOSR/AOARD), Australian Research Council, Toyota InfoTechnology Center, and Australian Institute of Sport. His research interests are in the areas of isolation kernel, isolation distributional kernel, ensemble approaches, data mining, and machine learning.

Prof. Ting is a member of program committees for a number of international conferences, including ACM SIGKDD, IEEE International Conference on Data Mining (ICDM), International Conference on Machine Learning (ICML), and ECML. He has served as a Senior Member for Program Committee for AAAI Conference for AI and PAKDD. He was a recipient of the Runner-Up Best Paper Award in 2008 IEEE ICDM, and the Best Paper Award in 2006 Pacific Asia Conference on Knowledge Discovery and Data Mining (PAKDD). He was the Co-Chair of the PAKDD in 2008.

Zhen Liu received the Ph.D. degree in computer application technology from the University of Electronic Science and Technology of China (UESTC), Chengdu, China, in 2007.

Since 2011, he has been an Associate Professor with the School of Computer Science and Engineering, UESTC. From 2012 to 2013, he was a Visiting Scholar with the Data Mining Laboratory, University of Minnesota, Minneapolis, MN, USA. During his academic career, he has authored more than 30 peer-reviewed articles. His research interests include data mining and analysis, machine learning, and social network analysis.

Bin He received the Ph.D. degree in computer and automation from Beijing Institute of Technology, Beijing, China, in 2001.

He is a Professor with Changchun Institute of Optics, Fine Mechanic and Physics, Chinese Academy of Sciences, Changchun, China. His research interests include space information processing, remote sensing image fusion, and analysis.